Electronic Supplementary Material (ESI) for Sensors & Diagnostics.

Supplementary Information

Real-time, smartphone-based processing of lateral flow assays for early failure detection and rapid testing workflows

Monika Colombo[1#] and Léonard Bezinge[1#], Andres Rocha Tapia[1], Chih-Jen Shih[1], Andrew J. deMello[1]* and Daniel A. Richards[1]*

[1] Institute for Chemical and Bioengineering, ETH Zurich, Vladimir-Prelog-Weg 1, 8093 Zürich, Switzerland
* Corresponding author: daniel.richards@chem.ethz.ch, andrew.demello@chem.ethz.ch
[#] Equal contribution

Table of Contents

S1 Statistical line detection

S1.1 Experimental setup

Fig. S1: Photograph of the modular setup with the mounted smartphone and eight strips inserted.

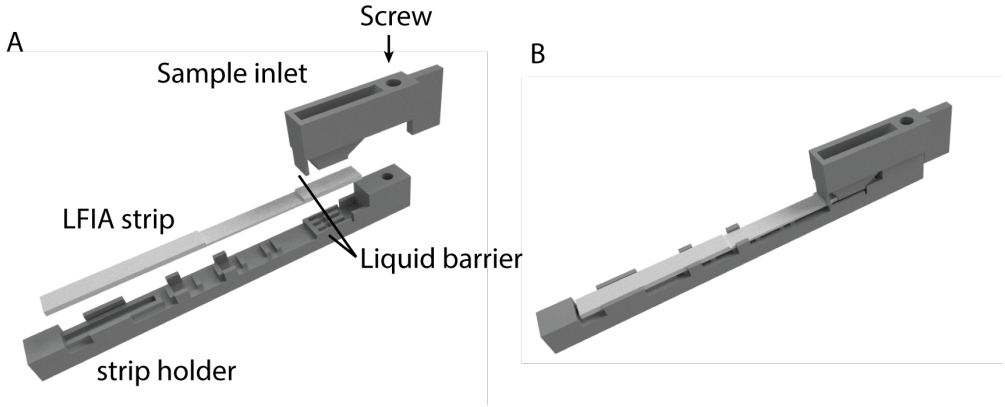

Fig. S2: Design of the strip holder. The holder accommodates a standard (4 mm wide) LFIA. The inlet has a 120 µL capacity and is tightened to avoid undesirable fluid leaking. Like a standard cassette, there are liquid barriers below the strip and after the inlet to force the liquid through the membrane and prevent overflow onto the membrane surface.

S1.2 Binding kinetics

We consider a bimolecular binding between (i) the gold nanoparticle immunocomplex and (ii) binding sites on the test line.[1] The differential equation describing the capture of the gold nanoparticle labels at the test line follows the Langmuir kinetic equation:

$$\frac{d\Gamma(t)}{dt} = k_{on} C_0 \, (\Gamma_{max} - \Gamma(t)) - k_{off} \, \Gamma(t) \tag{1}$$

With Γ being the surface concentration of bound particle, Γ_{max} the total surface concentration of binding sites, C_0 the concentration of the particles in solution entering the capture zone, and k_{on}/k_{off} the association and dissociation rate constants of the binding reaction. The concentration of available binding sites at a given time is given by $\Gamma_{max} - \Gamma$. We assume that the concentration of particles in flow C_0 is constant in time as it continuously enters the reaction zone.[2]. Further, assuming that no particles are bound on the test line initially ($\Gamma(0) = 0$), the solution to this first-order differential equation is:

$$\Gamma(t) = \frac{k_{on}\Gamma_{max}C_0}{k_{on}C_0 + k_{off}}[1 - \exp(-(k_{on}C_0 + k_{off})t)] \tag{2}$$

At sufficiently long times ($t \to \infty$), the final concentration of bound nanoparticles is given by the Langmuir adsorption model ($K_D = k_{on}/k_{off}$ is the dissociation constant):

$$\Gamma_\infty = \frac{k_{on}C_0}{k_{on}C_0 + k_{off}}\Gamma_{max} = \frac{\Gamma_{max}C_0}{C_0 + K_D} \tag{3}$$

Conversely, at early times, the equation can be simplified to a linear approximation ($1 - \exp(-x) \cong x$) with

$$\Gamma(t) = k_{on}\Gamma_{max}C_0 \, t = \text{const} \cdot C_0 \, t \tag{4}$$

Therefore, assuming that a signal is detectable once a certain threshold concentration of bound particle is reached
($R_t = \Gamma/\Gamma_\infty$), the threshold time t_t is given by:

$$t_t = \frac{R_t}{k_{on}C_0} = \frac{\text{const}}{C_0} \tag{5}$$

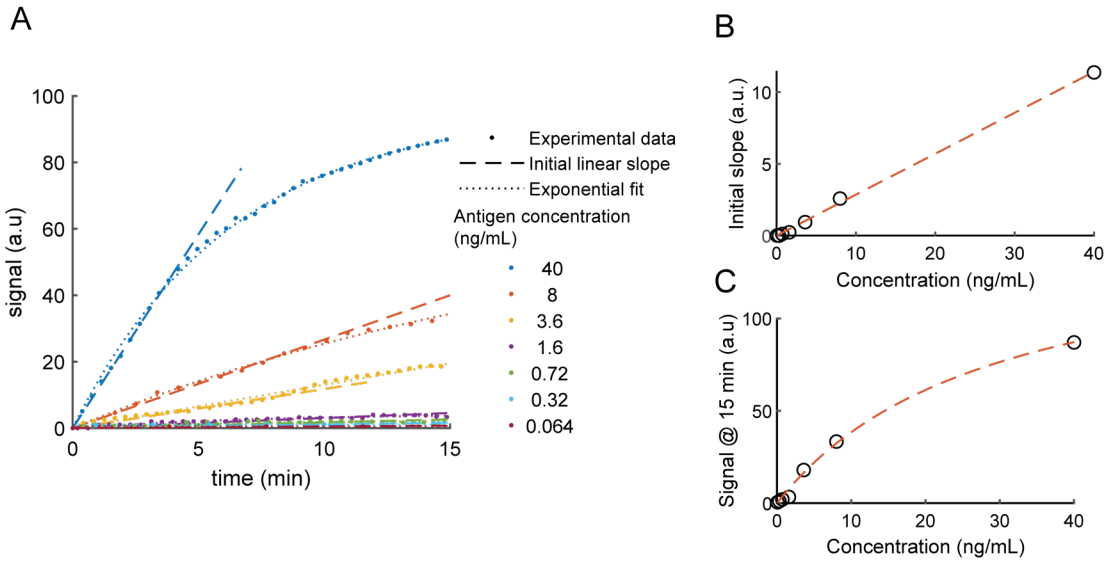

Fig. S3: (A) Binding curves from the analysed test line intensities with decreasing antigen concentrations. The curves exhibit an exponential character typical of pseudo first-order kinetics. **(B)** The initial slope is linearly proportional to the antigen concentration, while the final signal **(C)** follows a Langmuir adsorption model (Equation 3).

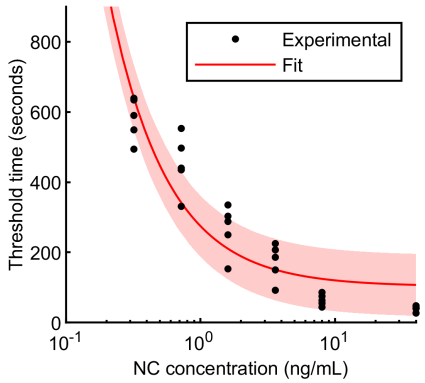

Fig. S4: The dependence of threshold times on the antigen concentrations can be approximated using an inverse relationship according to Equation 5.

S1.3 Case study high-throughput testing

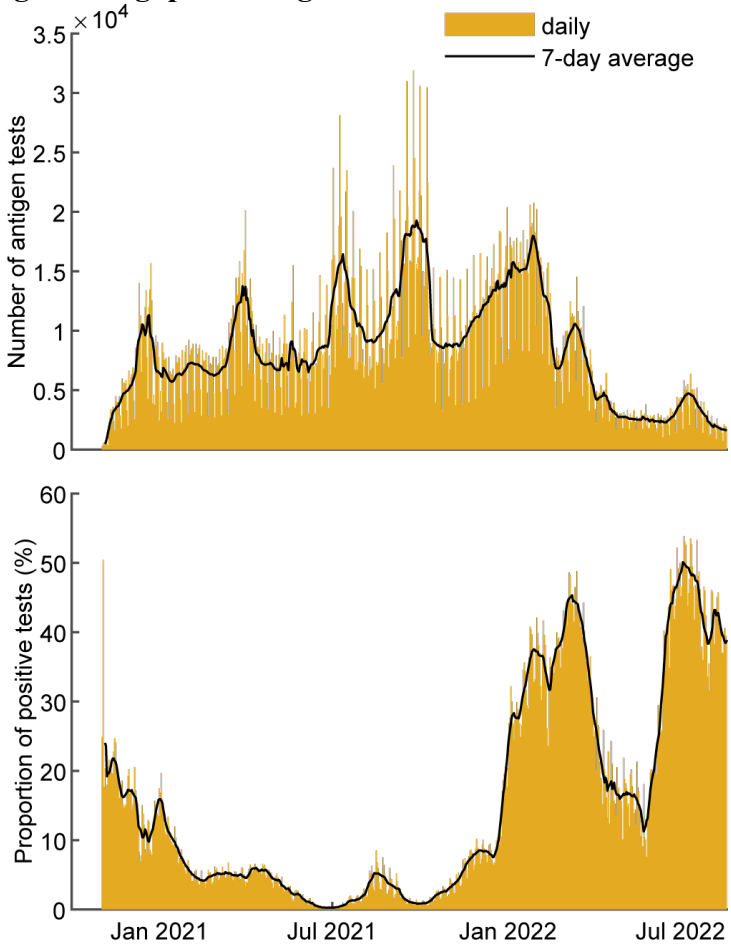

Fig. S5: Number of rapid antigen tests **(A)** and proportion of positive tests **(B)** during the COVID-19 pandemic in Switzerland. The daily values and the 7-day rolling average are displayed. The first week of July 2022 marked the highest rate of positive tests with a proportion >50 %. (Data from the Swiss Federal Office of Public Health, https://covid19.admin.ch).

S2 Early failure detection

S2.1 Identification of failure scenarios

Considering the entire life cycle of an LFIA test, common causes of failure arise from issues related to 1) manufacturing, 2) storage or (3) user operation. Below, we discuss potential causes of failures linked to these three categories and their effects on the operation of LFIAs.

Manufacturing. Despite their simple design, manufacturing LFIAs requires precise procedures to ensure consistent operation and reliable performance. Common failures related to improper manufacturing include misalignment or poor contact between the pads (sample, conjugate or absorbent pads) and the membrane, and delamination or structural defects in the membrane itself.[3] Since these faults affect the interactions between the liquid sample and the membrane, it is reasonable to assume they will disturb the flow profile. LFIAs rely on affinity binding to capture and label the target analyte. Thus, any issues during the printing of the capture line or with the conjugated nanoparticles labels may lead to false negatives, in the case of loss of affinity, or high background signals and false positives in the case of non-specific binding.[4] Fortunately, many of these issues can be detected by monitoring the control line. A weak signal at the control line could indicate defects in the printing of the control capture antibodies or the conjugation of the detection antibodies to the nanoparticles.

Storage. A major advantage of LFIAs is that they do not rely on the cold chain for transport and storage. According to the World Health Organization (WHO) Emergency Use List (EUL), LFIA tests must withstand 6 to 18 months of storage in dry conditions, with temperatures ranging from 4 to 30 °C.[5] Several failure risks arise with improper storage, including loss of affinity of the biological elements, poor resolubilisation of nanoparticles, and degradation of the nitrocellulose membrane. In these scenarios, we would expect to see differences in the flow profiles, background, and control line intensities – these could all easily be detected in real-time.

User operation. Sample collection for LFIAs is complex and varied, ranging from direct detection in urine (e.g. pregnancy tests), to swab sampling (e.g. COVID-19 antigen tests), to blood sampling (e.g. HIV tests). It is known that failure rates can be higher in self-tests performed by untrained users.[6] Certain failures caused by operator error, such as too much or too little sample volume, would result in disturbances to the flow profile and thus could be readily picked up by real-time imaging. Errors related to the inability of users to interpret the test lines are common,[6,7] and can be easily mitigated through automated image recognition.[8–10] Still, it is important to mention the limitations of real-time imaging with regard to user error. A significant source of user error in self-tests stems from improper sampling (e.g. insufficient rubbing of the nasopharyngeal swab).[11] In this scenario the tests run as designed, simply on improperly collected samples, and so there are no detectable changes in the operation of the tests.

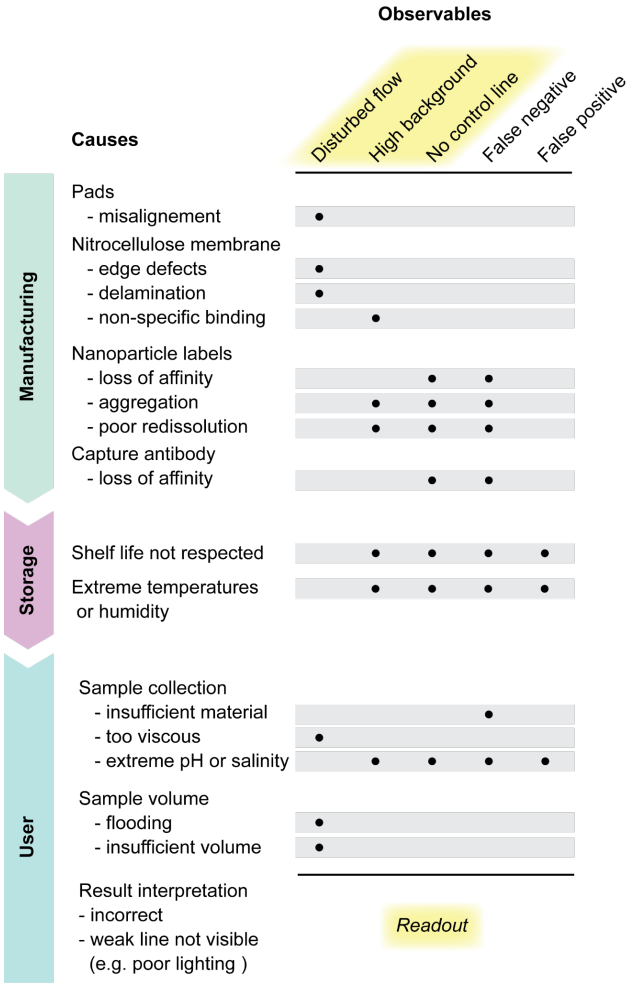

Figure S6. Assessing the failures in lateral flow assays. Failure points can arise on the entire life cycle of an LFIA test, and will lead to various observables, some of which (in yellow) can be detected through real-time imaging.

S2.1 Computational flow-front detection

In order to correctly process the movement of the wave front, the algorithm at each frame analyses the region of interest (ROI), namely the test strip defined through the *imcrop* function. As shown in Fig. S7 and S8, the wetting of the nitrocellulose paper induced a detectable difference in pixel intensity, even when converted to greyscale (MATLAB function *rgb2gray*, Fig. $S7_i$). Through automatic image adjustment (MATLAB function *imadjust*), the picture contrast is automatically increased (Fig. $S7_{ii}$). The Otsu criterion for thresholding (default option for *graythresh*) is used to further define the wave front edge through the function *edge* (Fig. $S7_{iii}$). Finally, the x- and y-coordinates of the detected edge are used to select the bounding box (returned by the *regionprops* function) of the wave front (Fig. $S7_{iv}$). It is worth noting that the edge point coordinates are crucial for the calculation of the wave front distortion, by analysing the distance of each single point from the averaged spatial distribution (Fig. S8).

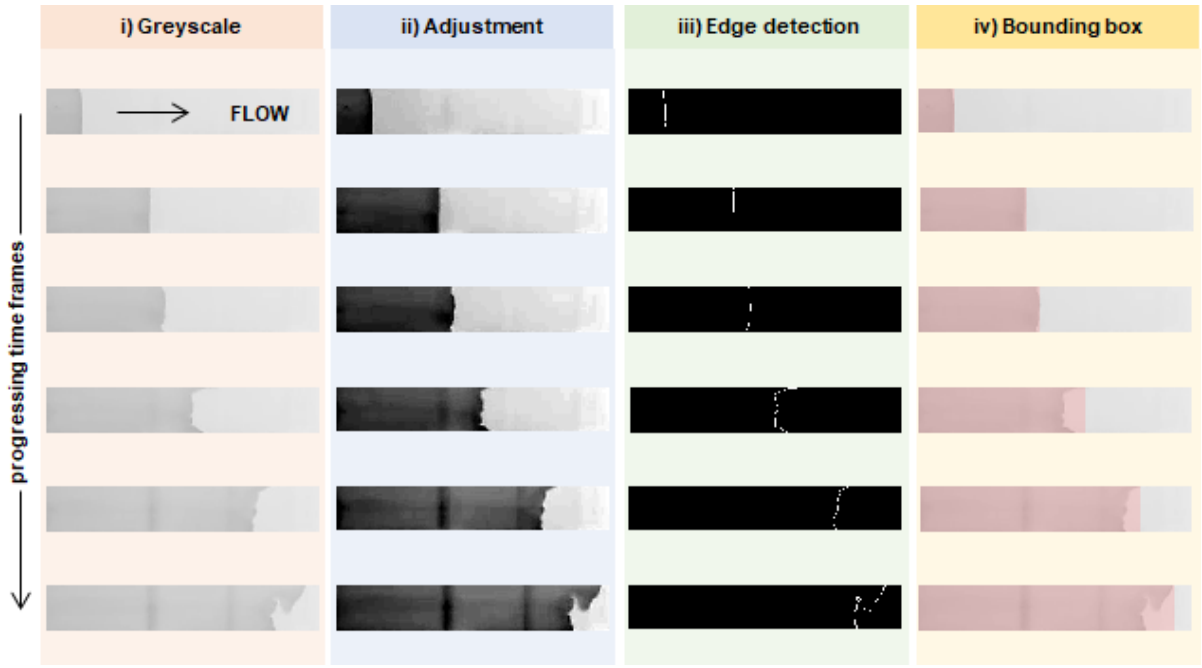

Fig. S7: Example of the detection of the advancing wave front. On the top left strip, the direction of the flow is indicated. i) At each time frame the strip image is converted to greyscale. (ii) Following image adjustment, the images are contrast adjusted to facilitate better edge detection of the flow front. (iii) The flow front (displayed in white) is traced along the vertical and horizontal direction. iv) An automatic bounding box is built around the furthest point of the front edge. Both the edge profile and position are used to compute the wave front distortion and to flag the presence of excessive wave front asymmetry.

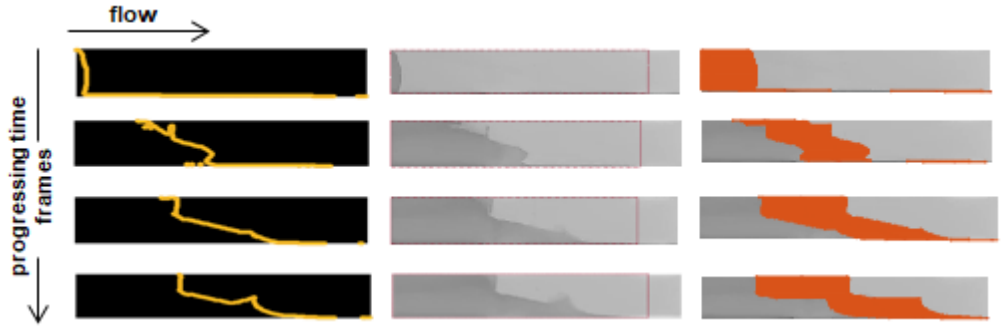

Fig. S8: Example of wave front advancement and detection in case of asymmetric and highly disturbed flow.

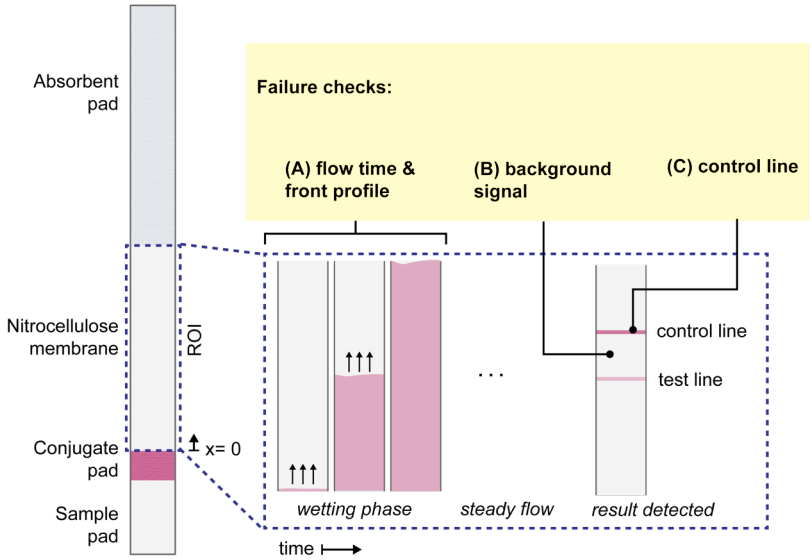

Fig. S9: Overview of the failure check procedure. The algorithm considers the region of interest (ROI) of the nitrocellulose membrane between the conjugate pad and the absorbent pad. The first failure check (A) occurs during the wetting phase and monitors flow time (defined as the time for the flow travel through the entire ROI) and front profile. If no perturbations in the flow rate or flow profile are detected, no failure is flagged and the algorithm proceeds to the statistical thresholding (continuous test line monitoring). Once a result is detected, the failure detection algorithm checks (B) the background signal and (C) the presence of the control line. If the background is within the defined limits and the control line is present the test is considered valid.

S3 Smartphone-based real-time parallel platform

To facilitate development of a smartphone App, the MATLAB algorithm was translated into C++. Since the recognition of the strip position is computed frame-by-frame, the automatic location of the ROIs is guided by the QR code identification (Fig. S9); this mitigates the impact of the slight movements during analysis.

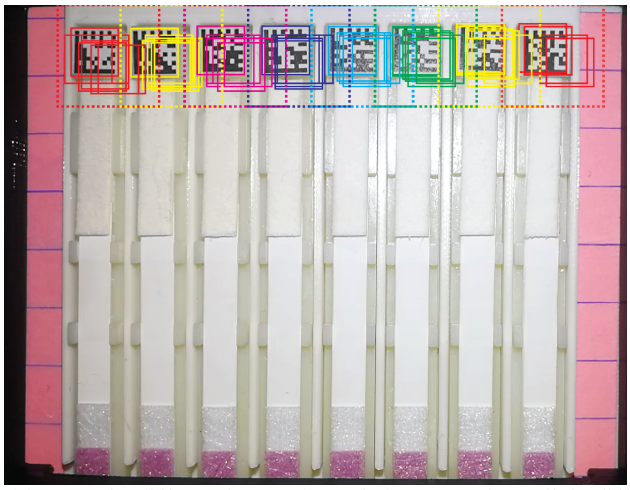

Fig. S10: Variation in strip positions on the different lanes. The variation stems from slight differences in smartphone positioning and is compensated by the app by calculating the various regions relative to the position of the detected QR codes.

Fig. S10 shows the demo of the developed smartphone App. Various LFIA tests were run, containing alternating negative, positive (strong and medium), or defective samples. Once the user has registered (Fig. S10A,B) they are instructed to start a new session (Fig. S10C). The App detects the QR codes and, after the sample is deposited and a fluid front is observed, the corresponding lane is shown as "running" (light blue, Fig. S10D). When the fluid reaches the end of the nitrocellulose paper, the early-failure modalities are checked and flagged when necessary, informing the user of an issue with the test (Fig. S10E). In this example, lane 2 ("Failed") is coloured in light orange, indicating an error in that strip (here, a disturbed flow resulting in an absent control-line). The other tests are under continuous evaluation and are coloured in a darker blue ("Running"). At the same time, the sample deposited on lane 8 has been detected as positive, and is thus flagged in red. In this case, the user can proceed to substitute the strip in lane 8 with a new test. In this case, another positive test was submitted in lane 8; the App detects this. Meanwhile, lane 4 is detected as "Positive", while lane 5 is flagged as "Failed" due to a slow flow-front. The lanes 1, 6 and 7, on which negative samples were initially deposited, are still flagged as "Running" (in dark blue). The negative results are confirmed (in green) only once the end-point has been reached (here 15 minutes) (Fig. S10H). Finally, the session can be stopped and the results saved in a database (.db) file that can be sent to the registered email address.

Fig. S11: Screenshots of the smartphone App during a run with mixed positive (strong and medium), negative, defective, or missing samples. Strips 1, 6, and 7 represent negative samples (buffer), strips 2 and 8 represent strong positive samples, and strip 4 represents a medium positive. Strip 5 represents a low-volume sample (30 µL instead of 120 µL), strip 3 is absent, and strip 2 was intentionally damaged resulting in a disturbed flow profile (flooding). **(A)** User registration; **(B)** New test registration; **(C)** Strips are inserted after sample deposition, and a new session is started; **(D)** During the initial stage of the run, the flow front and early-failure detection modalities are evaluated and missing lanes are flagged in grey; **(E)** Positive tests are flagged in red, while failed tests are flagged in yellow; **(F)** While changing strips (strip 8), the lane is temporarily flagged as empty until a new test is inserted; **(G)** All the positive samples are flagged, while evaluation of the negative samples continues until the end-point of the assay; **(H)** As the end point of the assay is reached, the negative samples are flagged in green. Once completed, the session can be stopped by the user and the results are stored on the device and also sent to the email address provided during registration.

References

1 D. Gasperino, T. Baughman, H. V. Hsieh, D. Bell and B. H. Weigl, *Annual Rev. Anal. Chem.*, 2018, **11**, 219–244.

2 D. V. Sotnikov, A. V. Zherdev and B. B. Dzantiev, *Biochemistry Moscow*, 2017, **82**, 1744–1766.

3 Merck Millipore, "Rapid Lateral Flow Test Strips, Considerations for Product Development", 2013.

4 C. Parolo, A. Sena-Torralba, J. F. Bergua, E. Calucho, C. Fuentes-Chust, L. Hu, L. Rivas, R. Álvarez-Diduk, E. P. Nguyen, S. Cinti, D. Quesada-González and A. Merkoçi, *Nat Protoc*, 2020, **15**, 3788–3816.

5 In vitro diagnostics detecting SARS-CoV-2 nucleic acid and rapid diagnostics tests detecting SARS-CoV-2 antigen, https://www.who.int/publications/m/item/PQDx-347-version-4, (accessed 12 October 2022).

6 C. Figueroa, C. Johnson, N. Ford, A. Sands, S. Dalal, R. Meurant, I. Prat, K. Hatzold, W. Urassa and R. Baggaley, *The Lancet HIV*, 2018, **5**, e277–e290.

7 C. C. Johnson, V. Fonner, A. Sands, N. Ford, C. M. Obermeyer, S. Tsui, V. Wong and R. Baggaley, *Journal of the International AIDS Society*, 2017, **20**, 21755.

8 R. A. Audu, R. N. Okoye, C. K. Onwuamah, F. A. Ige, A. Z. Musa, N. N. Odunukwe, D. I. Onwujekwe, O. C. Ezechi, E. O. Idigbe and P. J. Kanki, *African Journal of Laboratory Medicine*, 2015, **4**, 1–8.

9 T. Crucitti, D. Taylor, G. Beelaert, K. Fransen and L. Van Damme, *Clinical and Vaccine Immunology*, 2011, **18**, 1480–1485.

10 N. C. K. Wong, S. Meshkinfamfard, V. Turbé, M. Whitaker, M. Moshe, A. Bardanzellu, T. Dai, E. Pignatelli, W. Barclay, A. Darzi, P. Elliott, H. Ward, R. J. Tanaka, G. S. Cooke, R. A. McKendry, C. J. Atchison and A. A. Bharath, *Commun Med*, 2022, **2**, 1–10.

11 A. K. Lindner, O. Nikolai, F. Kausch, M. Wintel, F. Hommes, M. Gertler, L. J. Krüger, M. Gaeddert, F. Tobian, F. Lainati, L. Köppel, J. Seybold, V. M. Corman, C. Drosten, J. Hofmann, J. A. Sacks, F. P. Mockenhaupt and C. M. Denkinger, *European Respiratory Journal*, , DOI:10.1183/13993003.03961-2020.